Core-Double-Shell, CNT@Polypyrrole@MnO_2 Sponge as Freestanding, Compressible Supercapacitor Electrode

Peixu Li,[1] Yanbing Yang,[2] Enzheng Shi,[3] Qicang Shen,[4] Yuanyuan Shang,[3] Shiting Wu,[3] Jinquan Wei,[4] Kunlin Wang,[4] Hongwei Zhu,[4] Quan Yuan,[2] Anyuan Cao,[3*] Dehai Wu[1*]

[1] Department of Mechanical Engineering, Tsinghua University, Beijing 100084, P. R. China

[2] Key Laboratory of Analytical Chemistry for Biology and Medicine (Ministry of Education), College of Chemistry and Molecular Sciences, Wuhan University, Wuhan 430072, China

[3] Department of Materials Science and Engineering, College of Engineering, Peking University, Beijing 100871, P. R. China

[4] Key Laboratory for Advanced Materials Processing Technology and School of Materials Science and Engineering, Tsinghua University, Beijing 100084, P. R. China

*Corresponding authors. Email: anyuan@pku.edu.cn, wdh-dme@tsinghua.edu.cn

Supporting Information:

Table S1

Figure S1, Figure S2, Figure S3, Figure S4, Figure S5, Figure S6, Figure S7, Figure S8, Figure S9, Figure S10

Table S1. Weight change and PPy and MnO_2 mass content of the hybrid sponge samples (compared in Fig.4).

	Original CNT (mg)	After PPy coating (mg)	After MnO_2 coating (mg)	PPy mass content	MnO_2 mass content
CNT@PPy@MnO_2	1.12	1.79	2.94	22.8%	39.1%
CNT@PPy	1.06	1.39	——	23.7%	——
CNT@MnO_2	1.13	——	1.95	——	42.1%

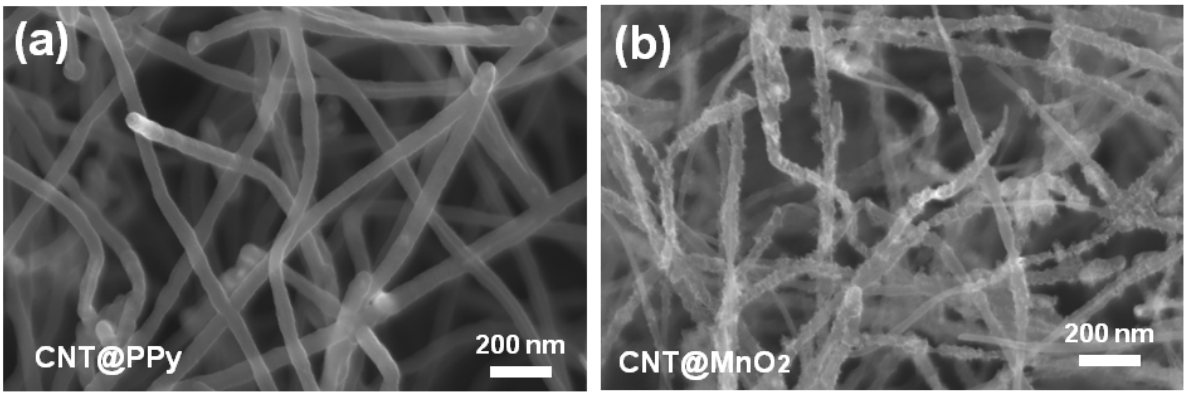

Figure S1. SEM images of CNT@PPy (a) and CNT@MnO_2 (b) core-shell sponges.

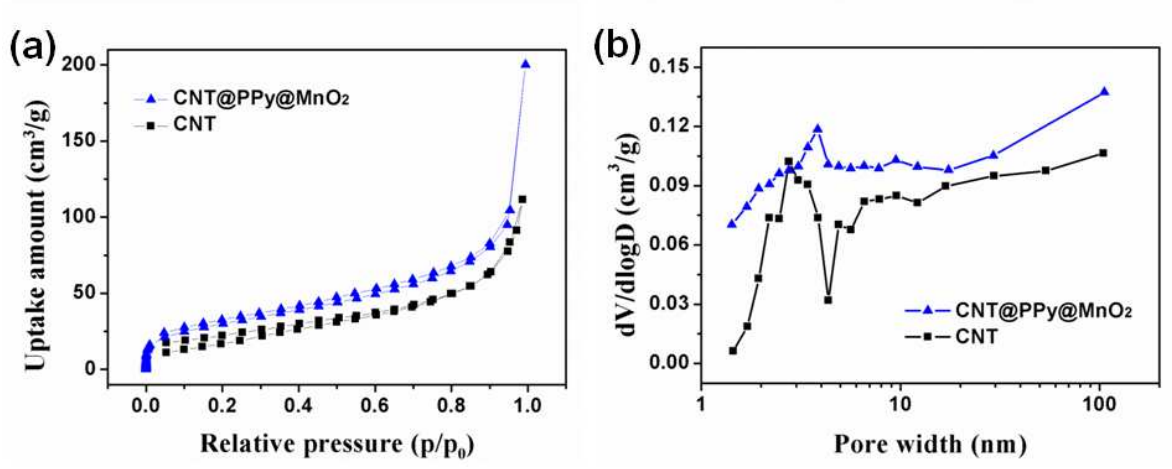

Figure S2. Nitrogen sorption isotherms and pore size distribution of CNT and CNT@PPy@MnO_2 sponges.

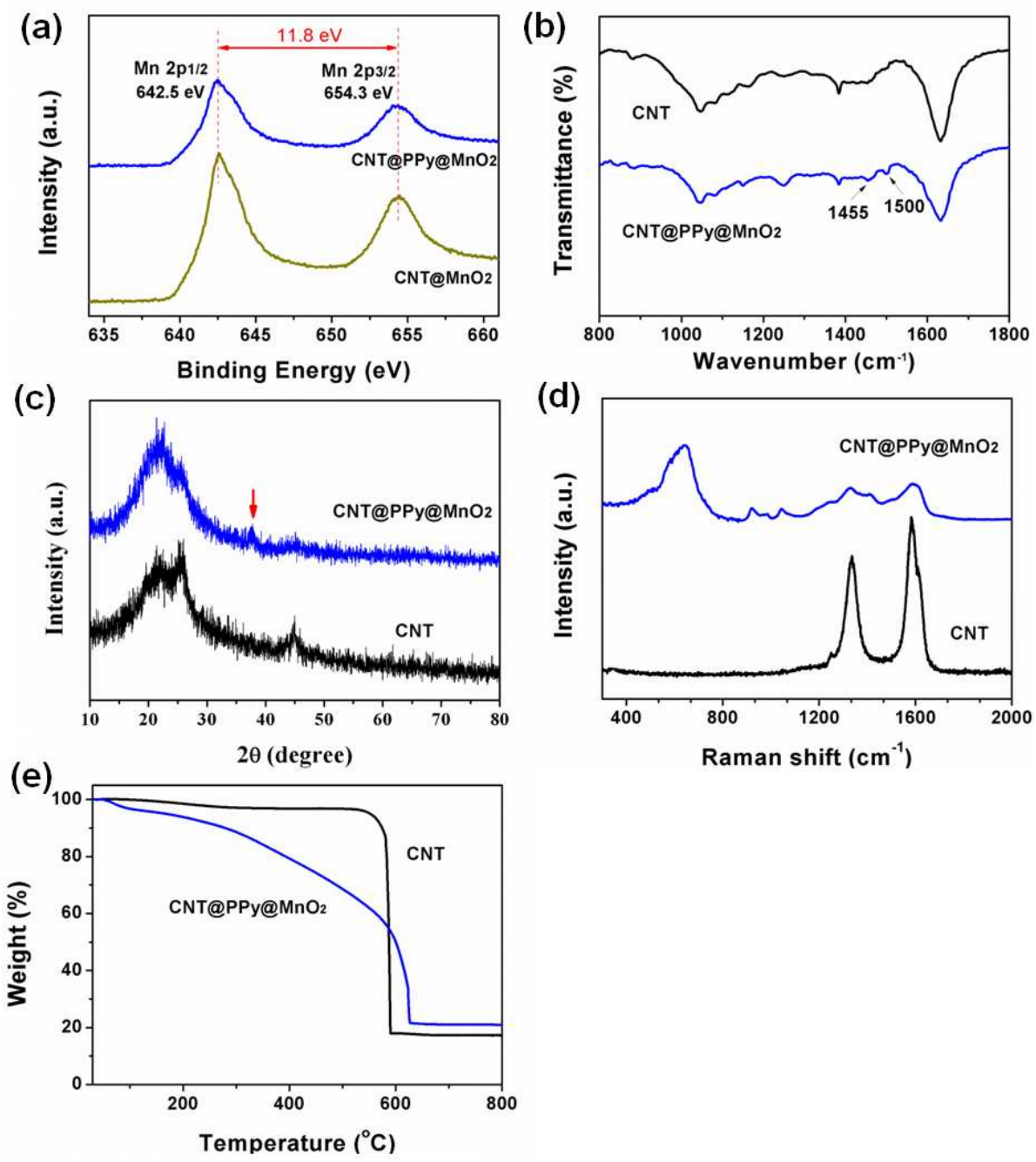

Figure S3. Characterization of the CNT@PPy@MnO_2 sponges by XPS, FTIR, XRD, Raman, and TGA.

Figure S3a shows the high-resolution Mn 2p core level XPS spectrum of CNT@PPy@MnO_2 and CNT@MnO_2 sponges. Mn $2p_{3/2}$ and Mn $2p_{1/2}$ have binding energies centered at 642.5 eV and 654.3 eV, respectively, with a spin energy separation of 11.8 eV.

Figure S3b shows the FTIR spectra of CNT@PPy@MnO_2 sponge which further verify the presence of PPy. The peaks at ca. 1500 and 1455 cm^{-1} in the CNT@PPy@MnO_2 sample can be

attributed to C-C and C-N stretching vibrations in the pyrrole ring, respectively.

Figure S3c shows XRD patterns of CNT and CNT@PPy@MnO_2 sponges. The CNT@PPy@MnO_2 sponge shows a characteristic peak at 37.5° (marked by an arrow), indicating the presence of MnO_2. Moreover, the weak peak features suggest that MnO_2 is in amorphous nature, which is favorable for supercapacitor applications.

Figure S3d shows the Raman spectra of CNT@PPy@MnO_2 sponge in comparison with the original CNT sponge. Raman spectra of the original CNT sponge show two characteristic peaks located at around 1584 (G-band) and 1337 cm^{-1} (D-band). The CNT@PPy@MnO_2 sponge exhibits the characteristic bands corresponding to CNT (1586 and 1332 cm^{-1}), PPy (920, 1043, and 1410 cm^{-1}) and MnO_2 (500-700 cm^{-1}).

Figure S3e shows TGA results on thermal stability of the CNT and CNT@PPy@MnO_2 sponges. TGA results show a higher weight loss temperature of the CNT@PPy@MnO_2 (625 °C) compared to the un-coated sponge (590 °C), indicating strong adherence of PPy and MnO_2 binary nanoshell which could delay the combustion of CNTs inside.

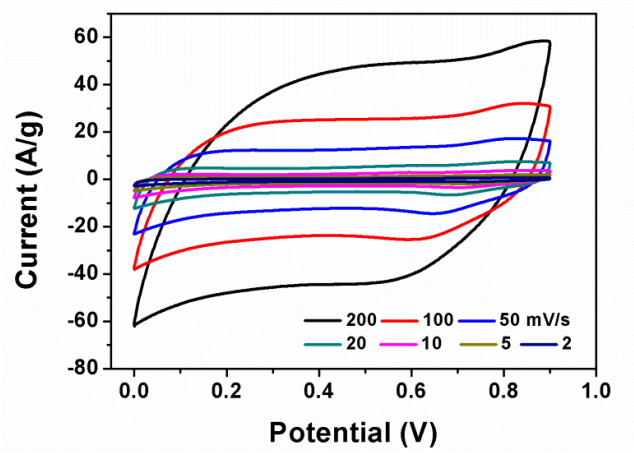

Figure S4. CV curves of a CNT@PPy@MnO_2 sponge measured in aqueous electrolyte at scan rates from 2 to 200 mV/s.

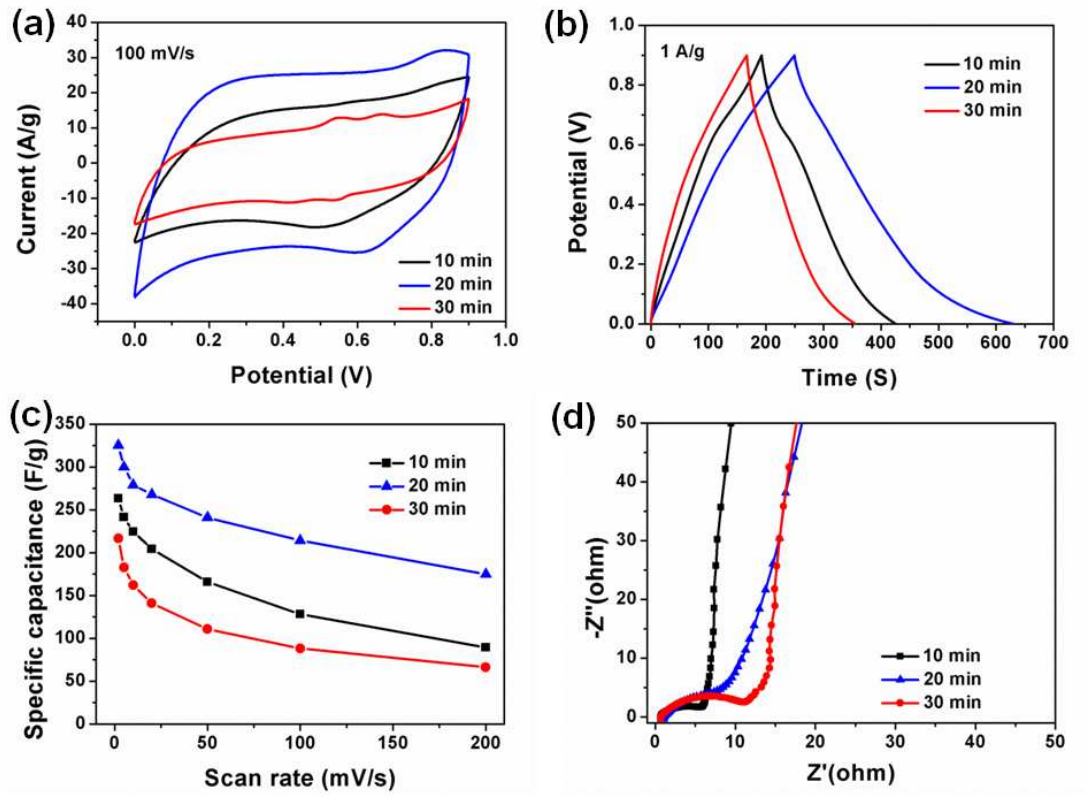

Figure S5. Supercapacitor performance comparison between the CNT@PPy@MnO_2 sponges by different hydrothermal synthesis periods (10, 20 and 30 min with corresponding MnO_2 loading of 26.3, 39.1 and 58.3 wt %). (a) CV curves of the three samples at a scan rate of 100 mV/s. (b) Galvanostatic charge/discharge curves of the three samples at a current density of 1 A/g. (c) Calculated specific capacitances of the three samples at different scan rates. (d) Electrochemical impedance spectroscopy of the three samples.

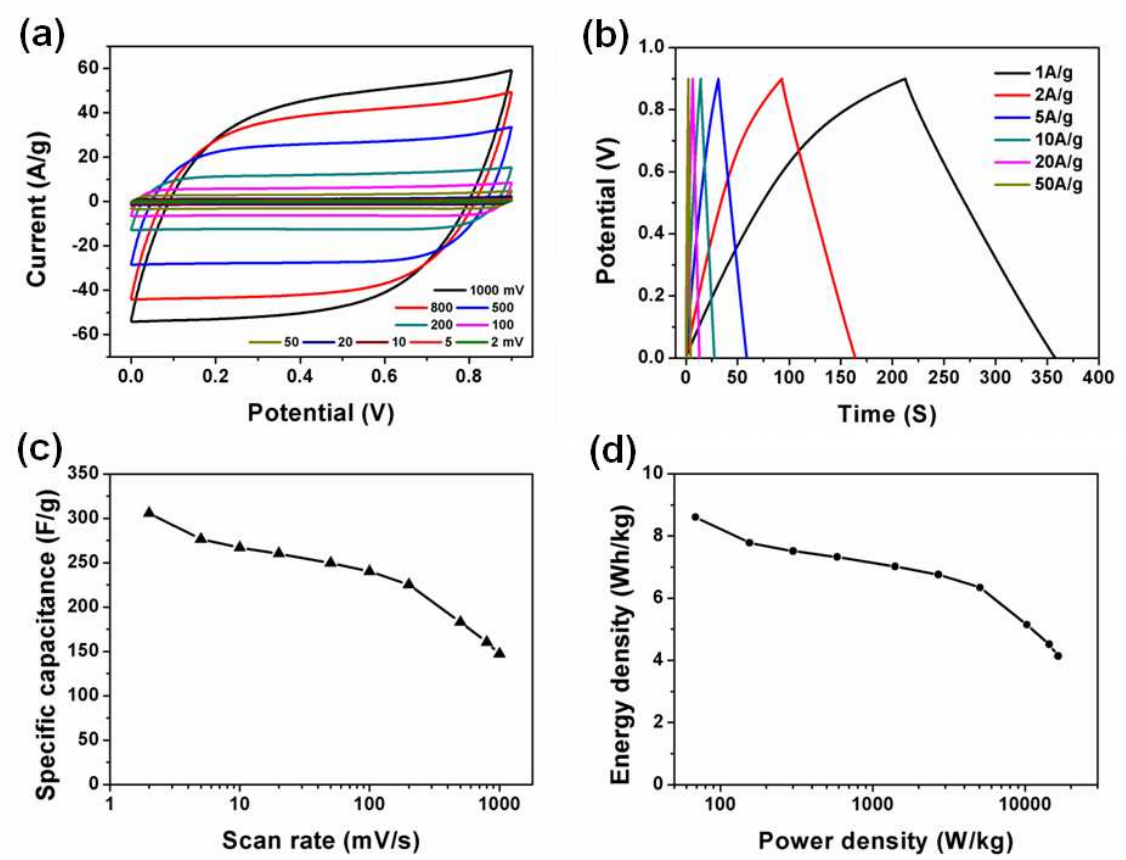

Figure S6. Supercapacitor performance of the CNT@PPy@MnO_2 sponge by the two-electrode configuration test. (a) CV curves of the supercapacitor at scan rates from 2 to 1000 mV/s. (b) Galvanostatic charge/discharge curves of the supercapacitor at current density from 1 to 50 A/g. (c) Calculated specific capacitances of the sponge electrode at different scan rates. (d) Energy and power density of the supercapacitor at different scan rates.

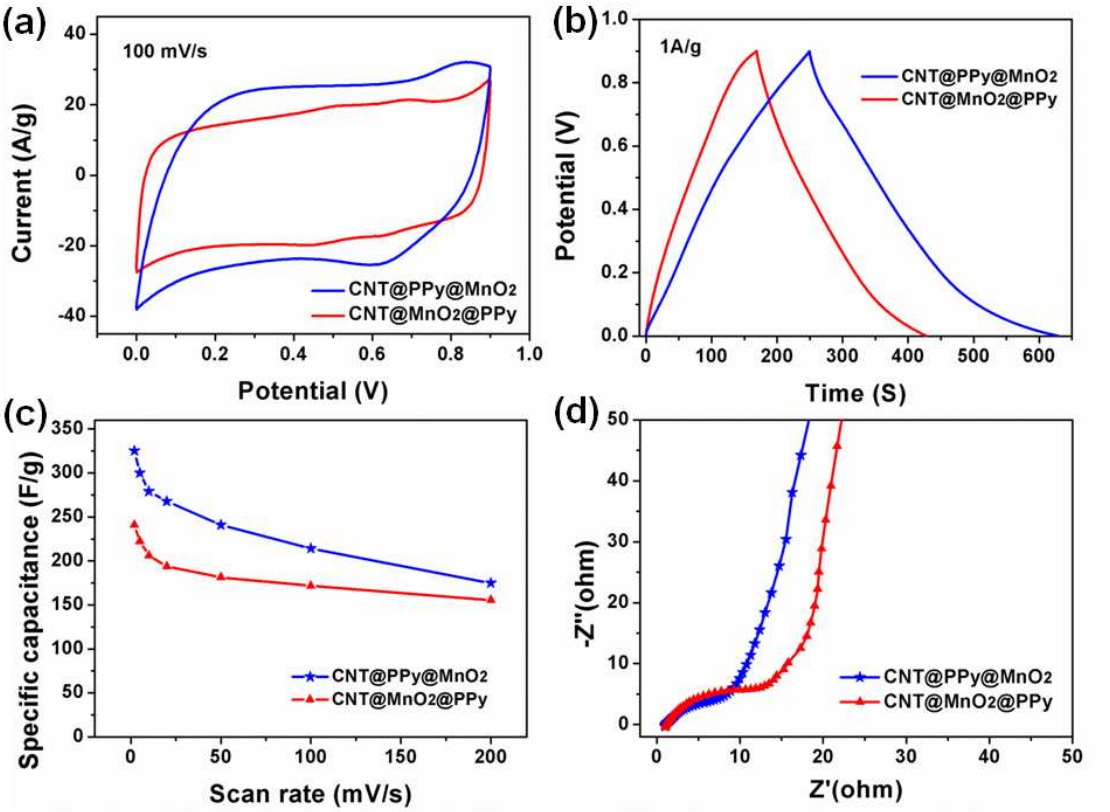

Figure S7. Supercapacitor performance comparison between the CNT@MnO_2@PPy and CNT@PPy@MnO_2 sponges (with ca. 40 wt % MnO_2 and ca. 20 wt % PPy). (a) CV curves of the two type sponges at a scan rate of 100 mV/s. (b) Galvanostatic charge/discharge curves of the two sponges at a current density of 1 A/g. (c) Calculated specific capacitances of the two sponges at different scan rates. (d) Electrochemical impedance spectroscopy of the two sponges.

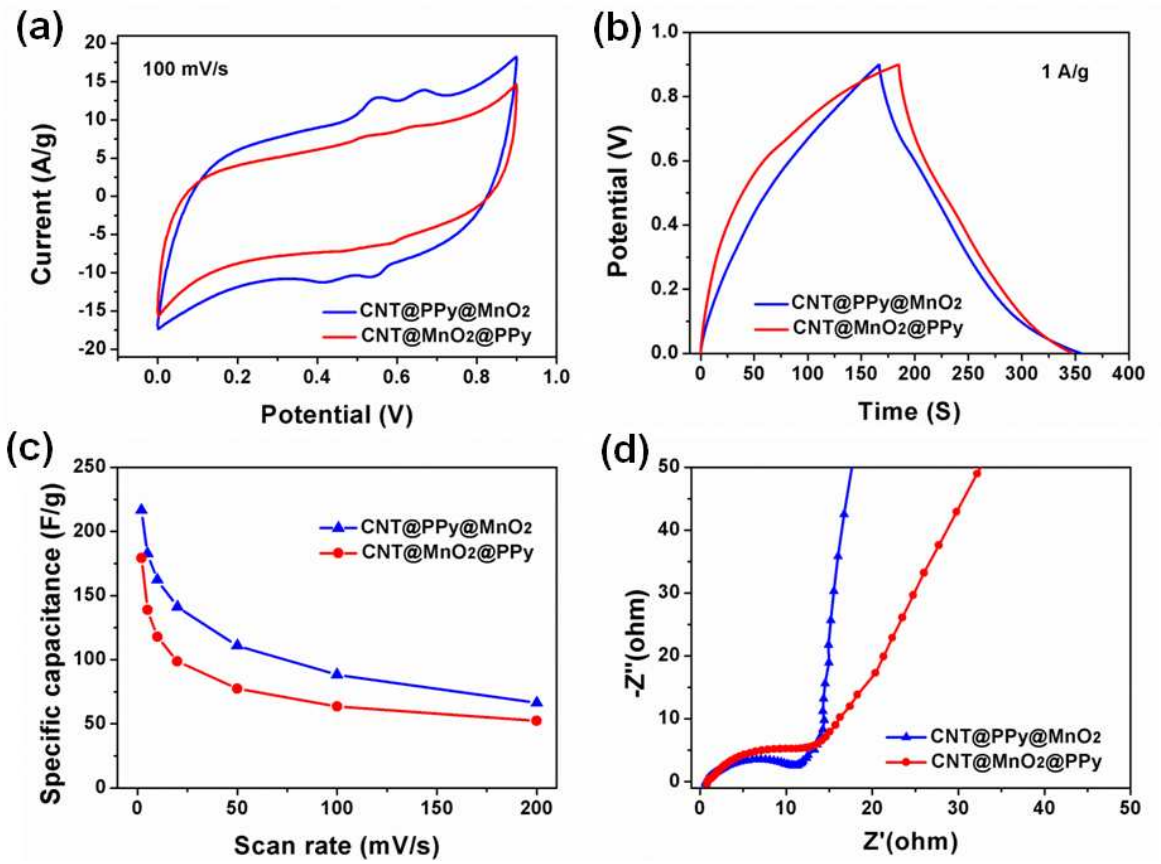

Figure S8. Supercapacitor performance comparison between the CNT@MnO_2@PPy and CNT@PPy@MnO_2 sponges with more MnO_2 loading (hydrothermal period for 30 min and ca. 58 wt % MnO_2). (a) CV curves of the two type sponges at a scan rate of 100 mV/s. (b) Galvanostatic charge/discharge curves of the two sponges at a current density of 1 A/g. (c) Calculated specific capacitances of the two sponges at different scan rates. (d) Electrochemical impedance spectroscopy of the two sponges.

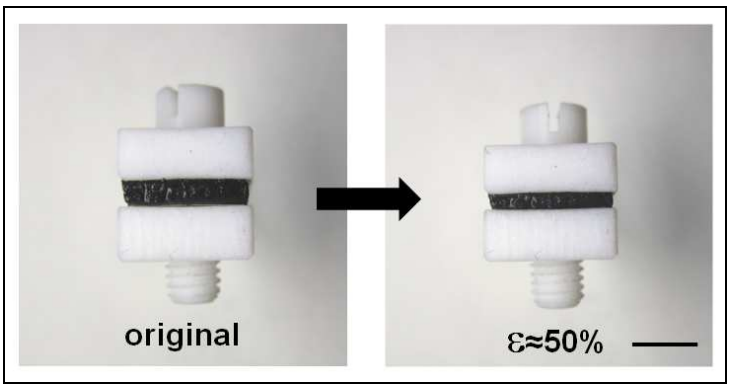

Figure S9. The CNT@PPy@MnO_2 sponge is clamped by specially designed clamp and can be compressed *in situ* controllably. The CV curves are recorded in the original and compressed states (ε=50%). Scale bar =5 mm.

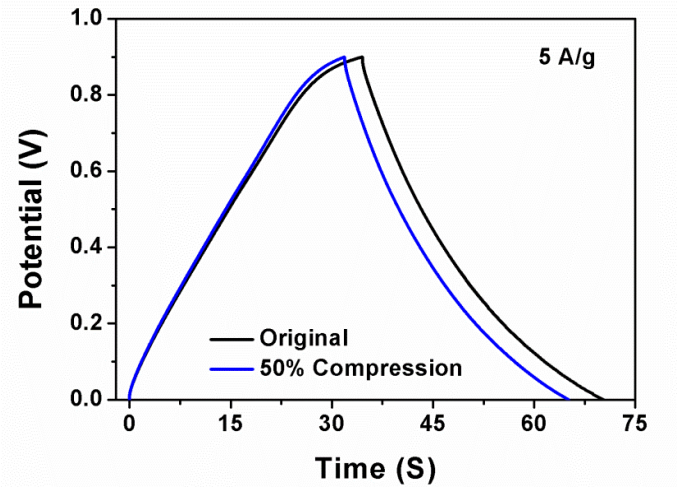

Figure S10. Galvanostatic charge/discharge curves of the CNT@PPy@MnO_2 sponge in original and compressed states at a current of 5 A/g.